Serb. Astron. J. № 166 (2003), 13 - 30 **UDC 524.82**
Original scientific paper

A MULTI-FREQUENCY STUDY OF THE DEEP PAVO FIELD

M. D. Filipović[1,2], M. Anderson[1,2], R. D. Ekers[2], I. J. Danziger[3], H-U. Zimmermann[4], G. L. White[2], P. A. Jones[2], B. C. P. Borun[1], J. L. Payne[1], M. Dionne[1], M. Ganis[1,5] and M. Ognjanović[1]

[1] *University of Western Sydney, Locked Bag 1797, Penrith South, DC NSW 1797 Australia*
[2] *Australia Telescope National Facility, CSIRO, P.O. Box 76, Epping, NSW 1710 Australia*
[3] *Osservatorio Astronomico di Trieste, Via Tiepolo 11, I-34131 Trieste, Italia*
[4] *Max-Planck-Institut für extraterrestrische Physik, Giessenbachstraße, D-85740 Garching, Deutchland*
[5] *Pace University, 861 Bedford Road, Pleasantville NY 10532, USA*

(Received: March 23, 2003; Accepted: April 25, 2003)

SUMMARY: We test the prediction of Hamilton and Helfand (1993) that faint radio selected galaxies are a new class contributing to the diffuse X-ray background (XRB) radiation. The test is based on the correlation of X-ray, optical and radio positions for sources detected in *ROSAT* ($S_{0.08-2.4\ keV} > 6 \times 10^{-15}$ erg cm^{-2} s^{-1}, 69 sources) and ATCA ($S_{1.42\,GHz} > 250$ μJy, 93 sources) observations of the *Einstein* Pavo field. A total of six ATCA radio sources inside the inner ring of the ROSAT image are located within 10″ of the *ROSAT* X-ray positions, with one associated by random chance. Hence, five of the X-ray population are radio-emitters. Four of these sources in common to radio and X-ray surveys are identified in optical frequencies from which one is a well known (ATCA J211544-675404) quasi stellar object (QSO). Another source (ATCA J211139-674902) can be seen at optical frequencies and therefore is very likely to be a QSO. Two more of these sources are clear Active Galactic Nuclei (AGN) candidates (ATCA J211217-674914 and ATCA J211451-680038). Radio and X-ray source ATCA J211420-680109= RX J211420-680108 is a galaxy cluster candidate. The remaining source, ATCA J211414-675052, is a star-forming galaxy candidate assuming it is not associated by random chance. Even though the statistical sample is small, this does not support the postulate that star-forming galaxies are significant contributors to the soft X-ray source population. This implies the contribution of radio emitting X-ray sources to the diffuse XRB at $S_{0.08-2.4\ keV} > 6 \times 10^{-15}$ erg cm^{-2} s^{-1} is at most a few per cent.

Key words. cosmology: diffuse radiation – galaxies: active – galaxies: Seyfert – radio continuum: galaxies – X-rays: galaxies.

1. INTRODUCTION

The type of sources that produce the diffuse X-ray background (XRB) radiation, discovered in 1962 (Giacconi et al. 1962), is an important question (Boldt and Leiter 1987; McCammon and Sanders 1990; Fabian and Barcons 1992) that requires an understanding of the sensitivities of the instruments

one uses to measure it. There have been many theories about the types of objects that create these X-rays ever since they were found. For example, the hypothesis that a hot diffuse intergalactic medium can produce the XRB is supported by the exact thermal bremsstrahlung (kT = 40 keV) shape of the 3-50 keV XRB spectrum (Marshall et al. 1980). If correct, this hypothesis would indicate that hot electrons in the intergalactic medium should distort the cosmic microwave background spectrum via Compton scattering (i.e., the SZ effect). However, *COBE* measurements (Mather et al. 1990) show deviations from the microwave background black-body spectrum are too small, placing severe limits on the contribution of a diffuse hot plasma. Hence, the observed characteristics must result from the integrated emission of large numbers (i.e., a few thousand per square degree) of discrete X-ray emitters at all cosmic epochs.

The *Einstein* observatory pioneered the use of very deep pointed observations (Giacconi et al. 1979a,b; Murray 1981; Hamilton, Helfand and Wu 1991; Primini et al. 1990, *Einstein* deep survey) of blank areas of sky, at high galactic latitudes, to resolve the faint 1–3 keV XRB into as many discrete sources as possible. The 10 *Einstein* deep fields are estimated to resolve ∼16%–25% (Primini et al. 1990) of the XRB above a flux limit of 8×10^{-14} erg cm^{-2} s^{-1} (0.8-3.5 keV). Deeper *ROSAT* observations (summarized by Hasinger, Trümper and Schmidt 1991; Hasinger 1993; Hasinger et al. 1998) are estimated to resolve 70%-80% of the XRB into discrete sources to a flux limit of 1×10^{-15} erg cm^{-2} s^{-1} (0.5-2.0 keV).

Hamilton and Helfand (1993) cross-correlated 2σ fluctuations in two deep *Einstein* IPC images (0.3–3.5 keV) with deep Very Large Array (VLA) radio images ($S_{1.47\ \mathrm{GHz}}$ >150 μJy), finding 20% of the fluctuation are associated with mostly sub-mJy radio sources. Sources were considered to be coincident if they were separated on the sky by less than $1'$, the *Einstein* IPC instrumental resolution. They interpreted the finding as evidence for an emerging population of starburst-like, Narrow Emission Line (NEL) X-ray galaxies at faint X-ray fluxes ($\sim10^{-14}$ erg cm^{-2} s^{-1}). This conclusion follows from the observations of Benn et al. (1993) showing the majority of optical counterparts ($m_b < 22$) for sub-mJy radio sources have spectra similar to those of *IRAS* star-forming galaxies. Hence, faint radio selected galaxies might be a new class of contributor to the XRB.

Mushotzky et al. (2000) have shown with high sensitivity and spatial resolution *Chandra* X-ray observations that 75% of the hard XRB is resolved into discrete sources. Also, recent results from an X-ray survey of the *Chandra* Deep Field South (CDFS) indicate that there is still 20-40% (2-10 keV) of the XRB to be resolved (Giacconi et al. 2001). Recently, Tozzi et al. (2001) found in 300 ks exposure (2-10 keV) of the CDFS some 60-90% of the unresolved hard XRB. The remaining 10% might include some contribution from diffuse gas (the cosmic web, e.g. which is predicted to be about 5-10% of XRB) and some contribution from star forming galaxies at high (z>1) redshift. But in any case this contribution must be small. In the CDFS and other *Chandra* deep fields the emission from star forming galaxies seems harder than what is expected from star formation (winds plus high mass X-ray binaries). This suggests a low level nuclear activity responsible for X-ray emission rather than star formation. Therefore, the star formation rate predicted from hard X-rays is higher than that estimated from optical criteria for the same galaxies.

Hornschemeier et al. (2001) found 82 X-ray sources in the Caltech area down to limiting soft (hard) flux levels of $\approx1.3\times10^{-16}$($\approx6.5\times10^{-16}$) erg cm^{-2} s^{-1}. Sixty two soft-band sources account for more than 90% of the soft X-ray background and at faint fluxes they note the emergence of a population of apparent "normal" galaxies, including moderately star-forming ones. The latter population is only apparent in *Chandra* surveys with observation lengths longer than 100 ks. They detected (hard and soft X-ray bands) 16 correlations to sub-mJy radio sources (at 1.4 GHz) with 11 classified as "starburst-type". However, they are found that the high X-ray luminosities ($\geq5\times10^{42}$ergs s^{-1}) and large band ratios of several of the starburst-type systems strongly suggest that they contain previously unrecognized AGNs. In addition, there are only two "starburst-type" systems out of the eleven with Band Ratio's (hard to soft) $\leq$0.59. Nine low X-ray luminosity galaxies were listed in the optical data of (Hornschemeier et al. 2001, Table 6). This is plausibly explained by moderate strength starbursts, hot gas in elliptical galaxies, or other sources besides accretion onto a supermassive black hole. However, only one, $123634.5+621213$, they label as a starburst galaxy. Hornschemeier et al. (2001) also found that even deeper observations may reveal that AGNs cease to dominate the X-ray number counts at extremely faint soft-band fluxes in a manner analogous to the dominance of star-forming galaxies rather than AGNs at very faint radio flux densities. This is perhaps not surprising, as one would expect less luminous, nearby X-ray sources to appear as X-ray surveys achieve greater sensitivities. The question of the makeup of the XRB thus strongly depends on the sensitivity with which one measures it and whether non-accretion events such as starbursts (ultimately supernovae and binary accretion) contribute to it with significant energy.

Zamorani et al. (1999) presented X-ray and optical identifications for a deep ROSAT PSPC observation in the "Marano field" detecting 50 X-ray sources with $S_{0.5-2\ \mathrm{keV}} > 3.7\times10^{-15}$ erg cm^{-2} s^{-1}, within the inner region of the ROSAT field ($15'$). Of the 42 reliable identifications there were 33 AGNs, two galaxies, three groups or clusters of galaxies and four stars. The galaxies and clusters were at lower X-ray flux levels. The Marano field was also observed by the ATCA at 1.4 and 2.4 GHz by Zamorani et al. (1999) with limits of 0.2 mJy at both frequencies.

Cross-correlation of the entire radio and X-ray catalogs produced four position coincidences within 10″. These corresponded to one radio galaxy, two AGNs, and possibly one NEL galaxy.

Optical identification (Danziger and Gilmozzi 1997; Shanks et al. 1991; Boyle et al. 1993) of the resolved X-ray emitters in the Pavo field is complete to $\sim 10^{-14}$ erg cm^{-2} s^{-1}. Active galactic nuclei (low luminosity AGN; mainly QSOs with some Seyfert galaxies) form the dominant population, accounting for ∼70%–80% of detected sources, with smaller contributions from clusters of galaxies (< 10%), galactic stars (< 10%, depending upon galactic latitude) and normal, or NEL galaxies (< 10%). This trend is reinforced by identification of fainter ROSAT sources in the same Pavo field by Danziger, Gilmozzi & Viezzer (in prep.). BL-Lac objects tend not to be detected due to their low sky density (Stocke et al. 1991) of 0.2 per deg^2 at $S_{0.5-2.0\ \mathrm{keV}} \geq 2\times10^{-14}$ erg cm^{-2} s^{-1} (i.e. better suited to wide angle surveys) or are overlooked due to the dominance of emission line objects in identified samples.

For deep radio surveys, optical identification programs show ∼50% of sub-mJy radio sources have optical counterparts with $m_b < 25$, reducing to ∼20%-30% for $m_b < 22$. Identified sub-mJy radio sources are mainly faint blue galaxies (Thuan and Condon 1987; Kron, Koo and Windhorst 1985; Windhorst et al. 1995), which tend to be clustered into small groups (Windhorst et al. 1995) and have disturbed optical morphologies probably caused by interacting, merging or star-burst galaxies (Kron, Koo and Windhorst 1985; Windhorst et al. 1995). The X-ray spectrum of these radio emitting galaxies should be hard if produced by a population of massive X-ray binary stars and supernova remnants formed from the star-burst activity. Hence, as a population they should be able to reproduce the observed (Marshall et al. 1980) hard XRB spectrum.

The CDFS has recently been observed with VLA by Kellermann et al. (2000). They found 20 radio sources within their 16×16 arcmin^2 area above 200 and 135 μJy at 1400 and 5000 MHz of which eight radio sources have an X-ray counterpart. Garrett (2001) observed the Hubble Deep Field with the European VLBI Network (EVN) and found three radio-continuum sources down to 4σ (168 μJy) level. The VLBA detections of all three sources suggest that most of the radio emission of these particular sources (including a 'dusty starburst') is generated by an embedded AGN.

Garrett et al. (2000) have presented high resolution EVN radio observations at 1.6 GHz showing that radio emission in the dusty starburst, VLA J123642+621331, arises mainly from AGN activity, suggesting that in this system both AGN and starburst activity co-exist.

Two radio surveys at 5000 MHz and 843 MHz covered the *Einstein* Pavo field (Table 1). Griffiths et al. (1983) surveyed the Pavo field using the Parkes 64-m radio telescope at 5000 MHz. Above the detection limit of 15 mJy (rms is 3 mJy) only one radio association was discovered ∼10″ from the X-ray position (source Nº 11 of Griffiths et al. 1983) and with flux density of 29±12 mJy. The optical identification is a QSO (z=1.13). The MOST Survey at 843 MHz (Bedding and Turtle 1990 hereafter BT90) assembled a mosaic of eight images covering the region of the Pavo field. The final 843 MHz image has an rms noise level of 0.43 mJy per beam, detecting 33 radio sources above 5σ=2.4 mJy. Cross-correlation of the X-ray and radio positions confirmed the previous association of Griffiths et al. (1983) with a QSO and found a marginal association (offset 38″) with a likely double lobed radio source.

Table 1. Summary of the X-ray and radio-continuum observations of the Pavo field.

Description	Value
RA field centre (J2000)	$\alpha = 21^h\ 14^m\ 24^s$
Dec field centre (J2000)	$\delta = -67^\circ 47' 24''$
Galactic Longitude	$b_{II} = -77^\circ$
Hydrogen column density	$N_H = (3.3\pm0.7)\times10^{20}$ atoms cm^{-2}

X-ray Telescope	X-ray Obs. Date	Exp ks	Reference
Einstein IPC		77	Griffiths et al. (1992)
Einstein HRI		320	Griffiths et al. (1992)
ROSAT PSPC	10 April 1991	27	This study
ROSAT HRI	3 May 1991	2	This study

Radio Telescope	Freq MHz	Beam Size	rms Noise mJy/b.a.	Reference
Parkes	5000	5′	3.0	Griffiths et al. (1983)
MOST	843	45″	0.43	BT90
ATCA	1416	6″	0.050	This study
ATCA	1680	6″	0.053	This study

The Pavo field (Griffiths et al. 1983, 1992; Danziger and Gilmozzi 1997) is the most sensitive *Einstein* Deep Survey field (Table 1). A 77 ks IPC (imaging proportion counter) image detected 17 sources, ∼38 per square degree. Four 80 ks *Einstein* HRI (high resolution imager) images covering the inner IPC field re-detected 16 sources, providing positions accurate to <10″. Griffiths et al. (1992) re-evaluated the original identifications proposed by Griffiths et al. (1983), revealing a composition of 11 AGNs, one elliptical galaxy (galaxy cluster), one emission line galaxy and four unknowns. Danziger and Gilmozzi (1997) reanalyzed the X-ray data (based on the work of Primini et al. 1990), detecting 15 of the original 17 sources and detected six new HRI and one new IPC sources down to a 3.5σ detection limit. Of the ∼22 sources detected, 19 QSO's, one elliptical galaxy (galaxy cluster), one NEL galaxy and one dMe star were found.

A *ROSAT* observation of the deepest *Einstein* field, the Pavo field, was completed in 1991/92, reaching a flux limit of $\sim 6\times10^{-15}$ erg cm^{-2} s^{-1}.

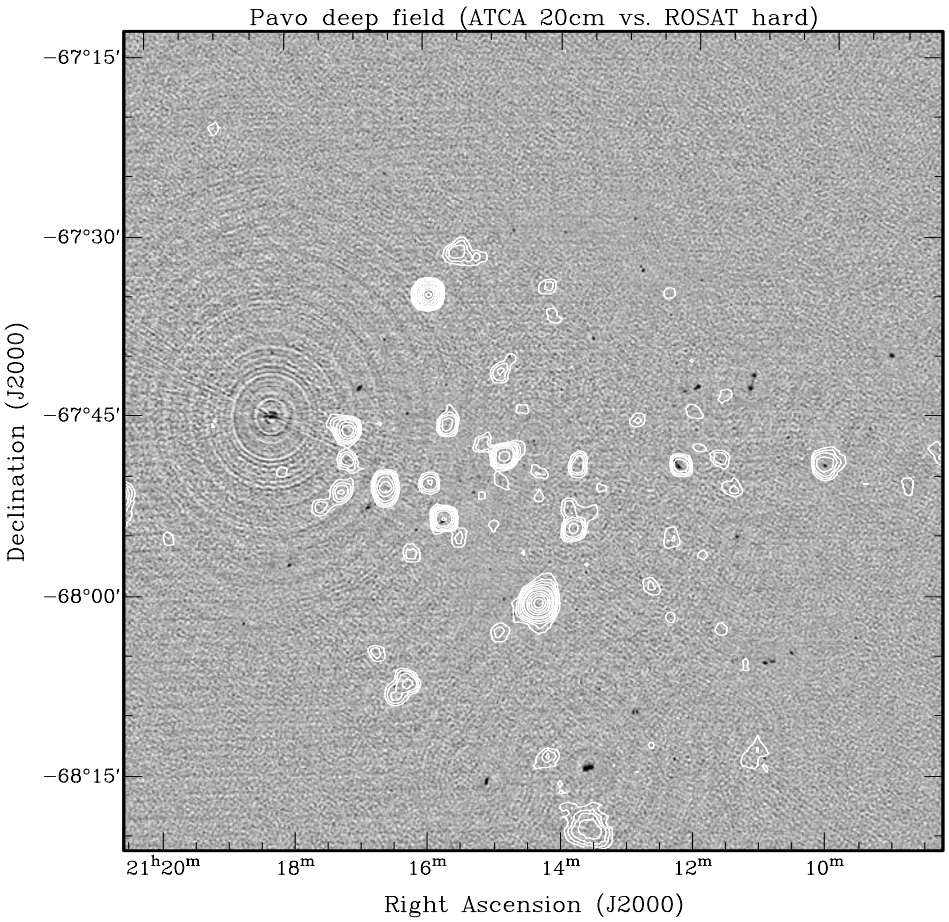

Fig. 1. *The ATCA 20-cm radio-continuum image (not primary beam corrected) of Pavo deep field (grey-scale) overlaid with contours from the ROSAT hard band observations. Note that the ATCA 20 cm resolution is 6″. Contours of the ROSAT image are: 1.3, 1.5, 1.7, 2, 2.5, 3, 4, 5, 6, 7, 8, 9 and 10 in units of 10^{-4} ROSAT PSPC counts s^{-1} $arcmin^{-2}$. Also note that there may be a correlation at ATCA J211006-674915, but this is outside of the inner ring of the ROSAT image and therefore was not used.*

(The basic properties of the Pavo field are listed in Table 1.) Our deep radio investigation is based on observations made with the ATCA at λ=20 cm. The low radio source density ensures a chance coincidence rate of <2% of spurious radio identifications for each X-ray error circle. The *ROSAT* position errors and the arcsecond radio positions allow for efficient optical identification. The degree of positional correlation between the X-ray and radio positions is used to test the prediction of Hamilton and Helfand (1993), combined with identification of the optical counterparts.

2. OBSERVATIONS

2.1. Radio-continuum data

The $\sim 20'$ radius field of view of a 1420 MHz (λ=20 cm) ATCA radio image (see Figs. 1, 2, 3 and 4) is well matched to the area covered by the *ROSAT* image. One of the selection criteria for the *Einstein* Pavo field was for it to be free of bright radio sources. Unfortunately, a bright 330 mJy radio source PKS B2113-679 is located 22′ from the field center. At this distance the ATCA primary beam sensitivity reduces the flux from 330 mJy to ∼55 mJy, but the final image is still likely to be dynamic range-limited.

Small movements of the primary beam on the sky caused by random single dish pointing errors (i.e. wind/thermal load) will cause the intensity of PKS B2113-679 to vary randomly. These variations are amplified by the position of PKS B2113-679 on a steep section of the outer primary beam pattern, introducing a side lobe pattern with a small random variation in intensity. The clean algorithm can only remove the non-random side lobe patterns of PKS B2113-679. Minimization of this effect by placing PKS B2113-679 in the first null of the primary beam is not realistic due to the 39′ distance of the null from the field center.

Images constructed from the PMN (Gregory et al. 1994) single dish survey at 4850 MHz were used to check for other bright sources within 60′ of

the field center. The position and peak flux of all fluctuations in the image were recorded. Using a spectral index of $\alpha = -0.8$ ($S \sim \nu^{\alpha}$) (–1.0±0.2 by our calculations for source Nº 92 as shown in Table 2.), a flux at 1420 MHz was calculated for each peak and then reduced in intensity using the ATCA primary beam sensitivity pattern. For PKS B2113-679, the corrected flux density calculated is ∼330 mJy (Wright et al. 1994 at 4850 MHz – 123 mJy) or Gregory et al. (1994, 116 mJy) in good agreement with the value of 322 mJy estimated from a power law fit to flux values in the Parkes Catalogue. After B2113-679 the next brightest source has a peak flux of <20 mJy. At this level the 55 mJy peak flux of PKS B2113-679 is the only bright source in the field likely to introduce artifacts into the image. Also, we used the PMN images to search for other sources in the Pavo field and found eight sources above 3σ noise level (15 mJy).

The ATCA carried out a deep 12 hour synthesis in the 6A configuration on 5 April 1992, using two 128 MHz bands (33×4 MHz channels) centered on the frequencies 1416 MHz and 1680 MHz. The pointing center was matched to the *ROSAT* position (RA(J2000)=$21^h14^m24^s$ and DEC(J2000)=–67°47′24″). During the observation radio interference from the *GLONASS* satellites affected the 1680 MHz band only for ∼30 minutes. Weather conditions proved to be good, with wind speeds keeping under 5 km hr^{-1}. All observations were completed at night when solar interference was minimal and wind conditions were more stable to keep the single dish pointing accuracy as high as possible.

Calibration and editing was completed in the MIRIAD data reduction package at the ATNF, based on standard procedures developed by Sault and Killeen (1999) and assumed a flux of 16.19 Jy (1416 MHz) and 15.61 Jy (1680 MHz) for the primary calibrator PKS B1934-638. Each frequency was then imaged (2048×2048, 2″ pixels) and cleaned (∼550 000 iterations to reach ∼4σ residuals). The bandwidth synthesis technique was used on channels 7 to 29 to restrict the effect of bandwidth smearing to the 4 MHz channel width. The final cleaned images reached an rms of 50 μJy (1416 MHz) and 53 μJy (1680 MHz) (Table 1).

The MIRIAD task IMSAD was used to detect all sources above flux cutoff, taken as 5σ for the both images before primary beam correction. Estimates of the rms in the field center and in areas far from bright sources was comparable to the expected value. Reliability of the 5σ (250 μJy) detections within 20′ of the field center is high. The chance of including spurious sources is minimal as the largest negative images pixel is -4.4σ. As we expect, some sources with very steep spectral index (α <–1.0 or α >+1.0) and fluxes are near detection cutoff (2-5σ) at one frequency may not be seen at the other frequency above 3σ level. We again used IMSAD with cut-off lowered to the 3σ limit to look at the peak intensities for some of these sources. Some 13 sources appeared at 1680 MHz images in this category and only four at 1416 MHz. With parentheses, we flag these sources in Cols. 6 and 7 (Table 2), and maximal pixel values were estimated within the area of the source. Due to the residual sidelobes, several spurious sources within 2′ of PKS B2113-679 have been excluded from the final source list. A small spurious peak due to the DC offset at the field centre was also excluded. Finally, after both images were primary beam corrected, flux densities were calculated using MIRIAD tasks IMFIT (for extended and point like sources) and IMSTAT (for very extended sources).

The final source list (Table 2.) includes 91 detected sources sorted into right ascension (RA) order. We also list positions for two additional sources detected very close to the edge of nominal primary beam. For these two sources (Nº 1 and Nº 10 in Table 2) we did not estimate flux densities since they are very uncertain. Therefore, the total number of radio sources in the Pavo deep field is 93.

2.1.1. Radio-Continuum Uncertainties in Flux Densities

We have compared the flux densities at our two close radio frequencies (1416 and 1680 MHz). This type of analysis gives the uncertainty in flux density in the form:

$$\Delta S = \sqrt{A^2 + (B \times S)^2} \qquad (1)$$

where A and B are constants. The flux-density-independent component of uncertainty *(A)* has been computed from the rms differences for weak sources (where flux-density-dependent uncertainties are negligible) and the flux-density-dependent uncertainties *(B)* have been computed from the rms differences for strong sources. For all but the very weakest sources, the uncertainty in flux density is dominated by the flux-density-dependent component which is ∼4%. For weak sources, the flux density uncertainties are dominated by the rms noise level giving uncertainties around 50 μJy.

Assuming a spectral index of α=–0.8, we expect that the change in flux density between two close frequencies (1416 and 1680 MHz) is ∼15%.

2.2. X-ray data

The *ROSAT* archive contains one pointed *ROSAT* PSPC and one HRI observation centered in the Pavo field. More details on the *ROSAT* mission can be found in Trümper (1982) and for more details of the PSPC observation of the Pavo deep field see Table 1. In Figs. 1 and 2, we show the *ROSAT* PSPC images (energy range 0.5 – 2.4 keV) of the Pavo field. It was obtained from PSPC observation, binned to 5″ pixels and smoothed for better representation. One *ROSAT* HRI observation was performed in the PAVO field but the low exposure time (2 ks) did not allow deeper quantitative study than was obtained from the PSPC observation.

The PSPC has a one degree wide field of view partially obscured by a support structure. Sensitivity is highest and off axis smearing minimal for the inner circular region of radius 20′. The outer region is subject to shadowing by the PSPC support struc-

Table 2. Measured ATCA properties of radio-continuum objects in the Pavo deep field. Flux densities in Col. 5 (S_{843}) are taken from BT90. Source BT32 from their catalogue could not be located in the ATCA data. Other MOST sources are not listed because they are blends of two or more ATCA sources. We flag with † in Cols. 6 and 7 sources found to be between 3 and 5 σ rms. The dash line in Cols. 6 and 7 represent sources which are just outside of the primary beam. With ( ), we flag sources which are found to be below 3 σ rms and for these sources the maximal pixel value were estimated within area of source. Spectral indexes are calculated if at least three (two if well separated in frequency) measurements above 5 σ rms are available for the source. Very extended points are labelled VE in Col. 11. For these very extended objects we estimate major/minor axis in arcsec.

(1) N$^{\underline{o}}$	(2) ATCA Source Name	(3) RA (J2000) h m s	(4) Dec (J2000) ° ′ ″	(5) S_{843} mJy	(6) S_{1416} mJy	(7) S_{1680} mJy	(8) $\alpha \pm \Delta\alpha$	(9) DSS2 m	(10) Count Rate cts ks^{-1}	(11) Ext	(12) Notes
1	J210846-675102	21 08 46.75	−67 51 02.8		—	—		19.1			
2	J210909-673958	21 09 09.71	−67 39 58.5		95.8	—					S_{4800}=42 mJy
3	J210927-674605	21 09 27.61	−67 46 05.1		6.1	—					
4	J210936-680333	21 09 36.39	−68 03 33.0		15.8	—					
5	J211006-674915	21 10 06.56	−67 49 15.1		10.0	11.6					
6	J211033-680454	21 10 33.68	−68 04 54.5		31.0	35.9					
7	J211039-674656	21 10 39.70	−67 46 56.0		3.2	3.7					
8	J211048-674835	21 10 48.29	−67 48 35.9		1.7	1.4					
9	J211049-680537	21 10 49.56	−68 05 37.6		8.0	10.4					
10	J211051-680541	21 10 51.77	−68 05 41.2		8.5	11.7					
11	J211056-681342	21 10 56.45	−68 13 42.2		—	—					
12	J211057-680545	21 10 57.67	−68 05 45.5		17.8	12.7					
13	J211111-674223	21 11 11.55	−67 42 23.5		17.2	16.2		20.5		VE	90″×20″
14	J211123-680531	21 11 23.12	−68 05 31.7		1.5	1.2					
15	J211123-675517	21 11 23.73	−67 55 17.0	9.4	5.3	5.8	−0.8±0.2				
16	J211126-680539	21 11 26.47	−68 05 39.4	6.9	2.7	(1.1)					
17	J211129-674725	21 11 29.34	−67 47 25.4		(0.1)	0.9					
18	J211137-673925	21 11 37.16	−67 39 25.7		(0.1)	0.9		15.6			
19	J211139-674902	21 11 39.42	−67 49 02.7		7.4	6.6		17.9	0.85±0.22		likely QSO
20	J211153-673855	21 11 53.90	−67 38 55.8		0.4	(0.1)					
21	J211157-673356	21 11 57.27	−67 33 56.4	3.8	1.9	(0.5)					
22	J211159-674253	21 11 59.59	−67 42 53.4	20.6	10.0	8.2	−1.3±0.2				
23	J211200-674623	21 12 00.80	−67 46 23.6		1.1	1.2					
24	J211202-674259	21 12 02.18	−67 42 59.9		4.3	4.1					
25	J211210-673951	21 12 10.74	−67 39 51.1		1.2	1.4					
26	J211211-674314	21 12 11.32	−67 43 14.5		1.8	1.9					
27	J211217-674914	21 12 17.91	−67 49 14.5		23.3	20.0			1.48±0.26	VE	74″×20″; AGN candidate
28	J211217-681351	21 12 17.66	−68 13 51.9		12.7	—					
29	J211218-674052	21 12 18.66	−67 40 52.1		0.8	†0.5					
30	J211221-674832	21 12 21.44	−67 48 32.3		0.4	0.4					
31	J211222-680230	21 12 22.41	−68 02 30.0		0.8	(0.5)		19.0			
32	J211223-673651	21 12 23.88	−67 36 51.7		1.0	1.3					
33	J211248-673309	21 12 48.68	−67 33 09.6	13.3	6.9	5.7	−1.2±0.2				
34	J211250-673250	21 12 50.65	−67 32 50.5		1.5	†0.9					
35	J211251-680957	21 12 51.64	−68 09 57.4	20.0	7.7	9.3	−1.3±0.4				
36	J211254-680145	21 12 54.70	−68 01 45.7		0.7	(0.5)		22.3			
37	J211255-681000	21 12 55.08	−68 10 00.5		6.4	8.0		22.3			
38	J211255-672851	21 12 55.70	−67 28 51.4		2.6	2.1					
39	J211325-680804	21 13 25.61	−68 08 04.8	4.9	2.9	3.8	−0.5±0.3	21.3			
40	J211331-673851	21 13 31.70	−67 38 51.8	4.5	3.4	3.0	−0.6±0.1	21.7			
41	J211335-681438	21 13 35.08	−68 14 38.9		195.2	190.3	−1.3±0.2			VE	S_{408}=1.03±0.15 Jy S_{4800}=35 mJy MRC 2109-684 56″×21″
42	J211337-675822	21 13 37.75	−67 58 22.7		0.8	0.6					
43	J211341-674533	21 13 41.33	−67 45 33.3		(0.1)	0.4					
44	J211341-680731	21 13 41.82	−68 07 31.6	2.9	2.9	(0.6)					
45	J211346-680129	21 13 46.07	−68 01 29.0		0.7	†0.5		17.9			
46	J211356-673000	21 13 56.55	−67 30 00.0		0.8	†0.8					
47	J211359-674310	21 13 59.73	−67 43 10.5		0.7	0.6					
48	J211405-674013	21 14 05.45	−67 40 13.2		0.4	0.3		18.1			
49	J211409-674049	21 14 09.24	−67 40 49.4		0.4	†0.3		20.7			
50	J211410-675731	21 14 10.10	−67 57 31.8		0.7	†0.6					
51	J211411-675013	21 14 11.67	−67 50 13.5		0.3	0.3					
52	J211414-675052	21 14 14.10	−67 50 52.0		0.4	(0.1)			0.92±0.30		possible Starburst Galaxy
53	J211418-674956	21 14 18.14	−67 49 56.1		0.3	0.3					
54	J211420-680109	21 14 20.80	−68 01 09.3		0.4	(0.2)		17.4	9.07±0.65		VMF98; 201 G Cluster
55	J211422-674758	21 14 22.31	−67 47 58.0		0.3	(0.1)					
56	J211433-674926	21 14 33.25	−67 49 26.6		0.5	0.4					
57	J211441-672949	21 14 41.61	−67 29 49.0	4.9	3.4	3.5	−0.5±0.1				
58	J211443-680153	21 14 43.21	−68 01 53.3	5.0	3.0	2.9	−0.8±0.1				
59	J211445-674024	21 14 45.86	−67 40 24.3		1.2	1.0		18.6			
60	J211445-673859	21 14 45.94	−67 38 59.4		0.4	†0.4		22.4			

Continued next page →

Table 2. (continued)

(1) N^{o}	(2) ATCA Source Name	(3) RA (J2000) h m s	(4) Dec (J2000) ° ′ ″	(5) S_{843} mJy	(6) S_{1416} mJy	(7) S_{1680} mJy	(8) $\alpha \pm \Delta\alpha$	(9) DSS2 m	(10) Count Rate cts ks^{-1}	(11) Ext	(12) Notes
61	J211451-680038	21 14 51.13	–68 00 38.8		1.3	1.2		21.8	0.59±0.17		AGN candidate
62	J211501-674911	21 15 01.65	–67 49 11.5		0.4	0.4					
63	J211502-675806	21 15 02.92	–67 58 06.9		0.9	0.7					
64	J211507-681547	21 15 07.04	–68 15 47.6		141.2	—	–1.1±0.2			VE	S_{4800}=35 mJy 36″ × 18″
65	J211517-675141	21 15 17.55	–67 51 41.8	2.7	1.9	2.0	–0.5±0.1	20.2			
66	J211526-674904	21 15 26.88	–67 49 04.9		0.3	(0.1)					
67	J211529-675043	21 15 29.21	–67 50 43.7		0.4	(0.1)		19.0			
68	J211532-675431	21 15 32.57	–67 54 31.0		1.1	1.3					
69	J211535-675425	21 15 35.81	–67 54 25.4		1.2	1.0					
70	J211541-674149	21 15 41.43	–67 41 49.7		0.3	0.3		18.7			
71	J211541-674244	21 15 41.29	–67 42 44.5		0.4	†0.2		20.1			
72	J211543-674457	21 15 43.79	–67 44 57.6		0.7	0.7		21.3			
73	J211544-675404	21 15 44.84	–67 54 04.1	55.5	21.4	20.9	–0.3±0.4	19.3	8.14±0.64	VE	S_{4800}=26 mJy HB89 2111-681 QSO 24″ × 18″
74	J211604-675122	21 16 04.70	–67 51 22.8	2.9	†0.5	0.5					
75	J211608-675447	21 16 08.70	–67 54 47.1	4.1	2.4	2.3	–0.9±0.1				
76	J211615-674507	21 16 15.92	–67 45 07.2	4.9	2.9	2.8	–0.9±0.1	20.1			
77	J211622-680644	21 16 22.12	–68 06 44.2	3.9	3.4	4.6	+0.1±0.2	17.8			
78	J211626-675049	21 16 26.60	–67 50 49.2	2.7	1.0	(0.2)					
79	J211629-680749	21 16 29.01	–68 07 49.9	2.5	3.0	2.8	+0.2±0.1	20.7			
80	J211634-672500	21 16 34.30	–67 25 00.2		3.0	2.6					
81	J211635-673854	21 16 35.26	–67 38 54.3	2.5	1.9	2.0	–0.4±0.1	20.4			
82	J211637-672821	21 16 37.00	–67 28 21.7		0.8	(0.5)		17.9			
83	J211638-675428	21 16 38.68	–67 54 28.0		(0.2)	0.7					
84	J211643-674626	21 16 43.60	–67 46 26.5		0.4	0.6					
85	J211644-675838	21 16 44.66	–67 58 38.3	2.6	1.3	1.8	–0.7±0.4				
86	J211651-675253	21 16 51.35	–67 52 53.3	51.0	29.7	27.9	–0.5±0.1			VE	S_{4800}=20 mJy 24″ × 18″
87	J211658-674258	21 16 58.22	–67 42 58.5	19.2	12.7	10.4	–0.9±0.1	20.0		VE	30″ × 20″
88	J211709-673422	21 17 09.31	–67 34 22.9	3.7	1.8	3.1	–0.5±0.5				
89	J211755-673920	21 17 55.39	–67 39 20.5	3.9	1.7	1.2	–1.7±0.1				
90	J211801-675736	21 18 01.71	–67 57 36.5	27.1	13.9	13.4	–1.1±0.2				
91	J211814-673953	21 18 14.08	–67 39 53.1	3.5	3.6	3.9	+0.1±0.1	20.9			
92	J211815-674513	21 18 15.32	–67 45 13.9	580	330.5	330.5	–1.0±0.2			VE	S_{4800}=106 mJy PKS 2113-679 42″ × 21″
93	J211843-680224	21 18 43.34	–68 02 24.9	31.5	11.7	10.7	–1.8±0.1				

ture and image degradation caused by significant off-axis smearing.

We detect X-ray sources down to a 3.5σ limit in the soft (0.1-0.4 keV), hard (0.5-2.0 keV), hard1 (0.5-0.9 keV), hard2 (0.9-2.0 keV) and broad (0.1-2.4 keV) PSPC bands. Any source detected in at least one band was included in the final source list, with positions taken from the band with the most significant detection. A total of 69 sources were in the final 3.5σ ($S_{0.08-2.4keV} > 6 \times 10^{-15}$ erg cm^{-2} s^{-1}) source list (Table 3). No attempt was made at this stage to detect sources beyond the inner circle of supporting structure (23′ from the centre of the Pavo field).

We catalogued all point-like and moderately extended X-ray sources found in the Pavo field in Table 3. The source positions were not corrected with respect to the positions of known standard sources (e.g. foreground stars or AGNs) because it may easily introduce improper shifts in position. A 90% source error radius was calculated, adding quadratically a 5″ systematic error.

$$P_e = 2.1 \times \sqrt{x_{\rm err}^2 + y_{\rm err}^2 + (5'')^2} \qquad (2)$$

The positional error derived for large off-axis angles $\Delta > 30'$ may be somewhat underestimated due to the asymmetry of the point-spread-function. However, the positional error should not be larger than ∼10″.

Column 1 gives the source catalogue number and Col. 2 the *ROSAT* source name. The X-ray source positions, RA and Dec, are given in J2000 coordinates in Col. 3 and Col. 4, respectively. The existence likelihood ratio (Col. 5) was calculated according to Cash (1979) and Cruddace, Hasinger and Schmitt (1988). Count rate (0.1-2.4 keV), hardness ratios (HR1) and (HR2) are given in Cols. 6, 7 and 8, respectively. HR1 is defined as HR1=(hard-soft)/(hard+soft) and HR2 is defined as HR2=(hard2-hard1)/(hard2+hard1) where soft, hard, hard1 and hard2 denote the PSPC count rates in the energy bands as defined above.

2.3. Optical Data

We use the Digital Sky Survey 2 (DSS2) optical red images of the Pavo field and UK Schmidt

Table 3. *ROSAT* PSPC properties of objects in Pavo field.

(1) N$^{\underline{o}}$	(2) Source X-ray Name	(3) RA (J2000) h m s	(4) DEC (J2000) ° ′ ″	(5) Existence Likelihood	(6) Count Rate (cts ks^{-1})	(7) Hardness Ratio HR1	(8) HR2
1	RX J211126-675123	21 11 26.40	–67 51 23.9	9.9	0.62±0.21	0.82±0.49	0.11±0.24
2	RX J211136-674401	21 11 36.94	–67 44 01.8	8.5	0.48±0.18	0.69±0.37	0.14±0.25
3	RX J211140-674900	21 11 40.12	–67 49 00.6	19.7	0.85±0.22	0.55±0.20	0.21±0.17
4	RX J211203-674505	21 12 03.46	–67 45 05.0	12.9	0.83±0.23	0.48±0.24	0.31±0.20
5	RX J211210-674106	21 12 10.23	–67 41 06.2	4.5	0.52±0.22	0.76±0.34	0.45±0.30
6	RX J211215-674914	21 12 15.44	–67 49 14.3	57.7	1.48±0.26	0.50±0.13	0.15±0.12
7	RX J211219-680259	21 12 19.61	–68 01 59.8	12.9	0.92±0.25	0.64±0.50	0.55±0.26
8	RX J211222-675530	21 12 22.92	–67 55 30.9	20.3	0.76±0.20	0.74±0.36	0.13±0.19
9	RX J211226-673514	21 12 26.46	–67 35 14.9	12.2	0.99±0.28	0.61±0.20	0.29±0.20
10	RX J211227-673725	21 12 27.11	–67 37 25.5	9.4	0.46±0.17	0.64±0.50	0.07±0.29
11	RX J211238-675959	21 12 38.94	–67 59 59.5	4.5	0.60±0.25	0.50±0.38	0.60±0.29
12	RX J211255-674546	21 12 55.57	–67 45 46.3	18.8	0.49±0.15	0.90±0.33	0.23±0.19
13	RX J211321-675145	21 13 21.73	–67 51 45.1	9.1	0.31±0.12	0.60±0.50	0.20±0.26
14	RX J211334-675301	21 13 34.78	–67 53 01.4	8.0	0.62±0.21	0.57±0.29	0.27±0.25
15	RX J211344-675047	21 13 44.20	–67 50 47.5	13.5	0.36±0.13	0.49±0.29	0.24±0.22
16	RX J211346-674927	21 13 46.25	–67 49 27.7	47.6	1.01±0.21	0.67±0.20	0.15±0.14
17	RX J211347-675416	21 13 47.87	–67 54 16.4	4.0	*	0.41±0.11	0.24±0.12
18	RX J211349-675456	21 13 49.54	–67 54 56.1	73.5	2.16±0.32	0.65±0.13	0.24±0.11
19	RX J211351-675303	21 13 51.95	–67 53 03.1	19.8	0.64±0.18	0.56±0.25	0.15±0.20
20	RX J211401-673808	21 14 01.52	–67 38 08.7	8.8	0.38±0.15	0.64±0.50	0.07±0.29
21	RX J211401-674659	21 14 01.94	–67 46 59.4	9.5	0.33±0.13	0.76±0.34	0.12±0.28
22	RX J211409-673705	21 14 09.92	–67 37 05.9	13.4	0.77±0.22	0.54±0.28	0.32±0.20
23	RX J211412-673442	21 14 12.74	–67 34 42.3	33.3	0.96±0.22	0.61±0.20	0.13±0.16
24	RX J211414-675201	21 14 14.80	–67 52 01.9	12.4	0.41±0.14	0.60±0.50	0.09±0.25
25	RX J211414-675046	21 14 14.81	–67 50 46.0	7.1	0.92±0.30	0.15±0.23	0.47±0.29
26	RX J211416-674237	21 14 16.44	–67 42 37.1	8.1	0.45±0.16	0.64±0.50	0.55±0.26
27	RX J211418-673915	21 14 18.85	–67 39 15.6	5.2	0.39±0.17	0.76±0.34	0.39±0.30
28	RX J211420-680108	21 14 20.51	–68 01 08.4	313	9.07±0.65	0.73±0.06	0.17±0.05
29	RX J211422-674951	21 14 22.50	–67 49 51.4	17.1	0.83±0.21	0.95±0.44	0.25±0.19
30	RX J211436-674500	21 14 36.83	–67 45 00.4	13.9	0.65±0.19	0.53±0.25	0.35±0.21
31	RX J211437-680042	21 14 37.29	–68 00 42.6	4.0	*	0.41±0.11	0.24±0.12
32	RX J211438-674829	21 14 38.46	–67 48 29.3	14.0	0.81±0.22	0.50±0.25	0.30±0.21
33	RX J211448-674045	21 14 48.93	–67 40 45.7	10.0	0.56±0.19	0.24±0.26	0.39±0.24
34	RX J211451-680032	21 14 51.30	–68 00 32.6	17.5	0.59±0.17	0.58±0.34	0.06±0.22
35	RX J211451-674853	21 14 51.38	–67 48 53.6	318.4	9.19±0.65	0.39±0.06	0.29±0.07
36	RX J211454-674201	21 14 54.22	–67 42 01.7	29.9	1.08±0.23	0.51±0.17	0.41±0.16
37	RX J211455-680346	21 14 55.12	–68 03 46.2	9.8	0.93±0.28	0.26±0.19	0.37±0.20
38	RX J211455-675057	21 14 55.73	–67 50 57.9	12.6	0.40±0.14	0.81±0.43	0.19±0.23
39	RX J211459-674632	21 14 59.69	–67 46 32.4	9.4	0.50±0.17	0.78±0.49	0.56±0.24
40	RX J211503-675433	21 15 03.89	–67 54 33.8	7.3	0.48±0.18	0.32±0.29	0.43±0.27
41	RX J211507-673224	21 15 07.49	–67 32 24.2	8.7	0.83±0.26	0.76±0.37	0.23±0.22
42	RX J211510-675216	21 15 10.22	–67 52 16.7	17.0	0.49±0.15	0.64±0.33	0.14±0.21
43	RX J211511-674746	21 15 11.21	–67 47 46.5	37.6	2.48±0.40	0.27±0.12	0.28±0.15
44	RX J211519-673231	21 15 19.94	–67 32 31.2	18.3	0.81±0.22	0.76±0.34	0.11±0.19
45	RX J211529-675424	21 15 29.74	–67 54 24.6	6.9	0.29±0.12	0.24±0.26	0.06±0.33

Continued next page →

Table 3. (continued)

(1) N^{o}	(2) Source X-ray Name	(3) RA (J2000) h m s	(4) DEC (J2000) ° ′ ″	(5) Existence Likelihood	(6) Count Rate (cts ks^{-1})	(7) Hardness Ratio HR1	(8) HR2
46	RX J211530-675537	21 15 30.58	–67 55 37.5	18.5	0.61±0.18	0.63±0.25	0.23±0.18
47	RX J211534-673150	21 15 34.15	–67 31 50.0	25.7	1.69±0.34	0.59±0.21	0.37±0.15
48	RX J211538-674510	21 15 38.20	–67 45 10.1	12.5	0.55±0.17	0.76±0.40	0.13±0.23
49	RX J211539-674614	21 15 39.43	–67 46 14.7	70.4	3.63±0.46	0.33±0.10	0.20±0.12
50	RX J211544-675403	21 15 44.33	–67 54 03.3	228.9	8.14±0.64	0.34±0.06	0.34±0.08
51	RX J211556-673523	21 15 56.73	–67 35 23.7	883.5	25.3±1.10	0.31±0.03	0.30±0.05
52	RX J211558-675100	21 15 58.07	–67 51 00.0	75.4	3.99±0.49	0.31±0.10	0.45±0.13
53	RX J211558-680234	21 15 58.24	–68 02 34.3	9.4	1.64±0.45	0.26±0.19	0.26±0.24
54	RX J211559-674018	21 15 59.84	–67 40 18.9	4.4	0.87±0.34	0.24±0.26	0.30±0.49
55	RX J211614-675702	21 16 14.36	–67 57 02.1	20.3	0.78±0.20	0.75±0.35	0.10±0.19
56	RX J211626-680743	21 16 26.70	–68 07 43.3	4.0	*	0.41±0.11	0.24±0.12
57	RX J211633-674330	21 16 33.21	–67 43 30.4	4.0	*	0.33±0.23	0.05±0.22
58	RX J211635-675201	21 16 35.65	–67 52 01.4	54.9	2.16±0.34	0.41±0.11	0.24±0.12
59	RX J211636-675103	21 16 36.34	–67 51 03.2	103.8	2.36±0.33	0.81±0.43	0.12±0.09
60	RX J211642-680443	21 16 42.22	–68 04 43.5	6.3	0.57±0.21	0.33±0.23	0.05±0.22
61	RX J211642-674625	21 16 42.60	–67 46 25.3	10.6	0.46±0.16	0.64±0.50	0.16±0.24
62	RX J211700-675016	21 17 00.80	–67 50 16.7	8.8	0.42±0.16	0.70±0.41	0.22±0.24
63	RX J211704-675616	21 17 04.45	–67 56 16.2	6.4	0.65±0.24	0.45±0.36	0.80±0.27
64	RX J211707-674633	21 17 07.96	–67 46 33.9	107.2	4.07±0.47	0.73±0.11	0.22±0.09
65	RX J211710-674911	21 17 10.56	–67 49 11.8	30.0	1.53±0.30	0.51±0.16	0.24±0.14
66	RX J211714-675143	21 17 14.64	–67 51 43.4	29.6	1.96±0.36	0.35±0.13	0.28±0.14
67	RX J211734-675303	21 17 34.30	–67 53 03.9	24.7	2.88±0.53	0.44±0.16	0.35±0.16
68	RX J211736-675303	21 17 36.67	–67 53 03.0	15.1	0.93±0.25	0.35±0.15	0.26±0.17
69	RX J211805-674954	21 18 05.38	–67 49 54.1	10.0	0.74±0.24	0.64±0.50	0.28±0.19

Telescope (blue) photographic data to identify our radio and X-ray sources (Fig. 4). We also use SuperCOSMOS database for radio/X-ray source identification. Looking into the lower-quality DSS1 data, taken 14 years earlier, we see that there are no large magnitude discrepancies, indicating that we do not have some transient bright source such as a supernova.

2.4. Total Hydrogen Column Density Estimate

We need to measure total hydrogen column density N_H to correct X-ray fluxes for galactic absorption. Values used by Griffiths et al. (1983) and Primini et al. (1990) are averaged values appropriate for the galactic latitude of Pavo field (b_{II}= –77°). Improved values (Table 4) have been determined using surveys that sample the H I (Cleary, Haslam and Heiles 1979; Colomb, Poppel and Heiles 1980) and dust (Schlegel, Finkbeiner and Davis 1998) distribution at the position of the Pavo field.

The H I single dish surveys of Cleary, Haslam and Heiles (1979, HPBW 48′, $\delta < -30°$) and Colomb, Poppel and Heiles (1980, HPBW 48′, $\delta < -30°$) have a pointing center located within 5′ of the Pavo field center. We used the published H I profiles to determine two independently measured N_H values (Table 4) of $\leq(3.3\pm0.7)\times10^{20}$ atoms cm^{-2} and $\leq(3.4\pm0.9)\times10^{20}$ atoms cm^{-2} respectively. As neither survey has corrected the observed H I profile for contamination from spillover or far field radiation, mainly from the galactic plane, the derived values are upper limit estimates only. To estimate an uncontaminated N_H value we used the correlation (Boulanger et al. 1996; Schlegel, Finkbeiner and Davis 1998) between the *IRAS* 100-μm dust maps and N_H.

Table 4. Summary of the N_H values for the Pavo field. CHH stands for Cleary, Haslam and Heiles (1979), CPH for Colomb, Poppel and Heiles (1980), DL for Dickey and Lockman (1990) and SFD for Schlegel, Finkbeiner and Davis (1998).

Data Source	N_H Value ($\times10^{20}$ atoms cm^{-2})	Survey Type
CHH	$\leq 3.3 \pm 0.7$	H I
CPH	$\leq 3.4 \pm 1.0$	H I
DL	2.2±0.8	H I
SFD	3.0±0.7	*IRAS* 100-μm

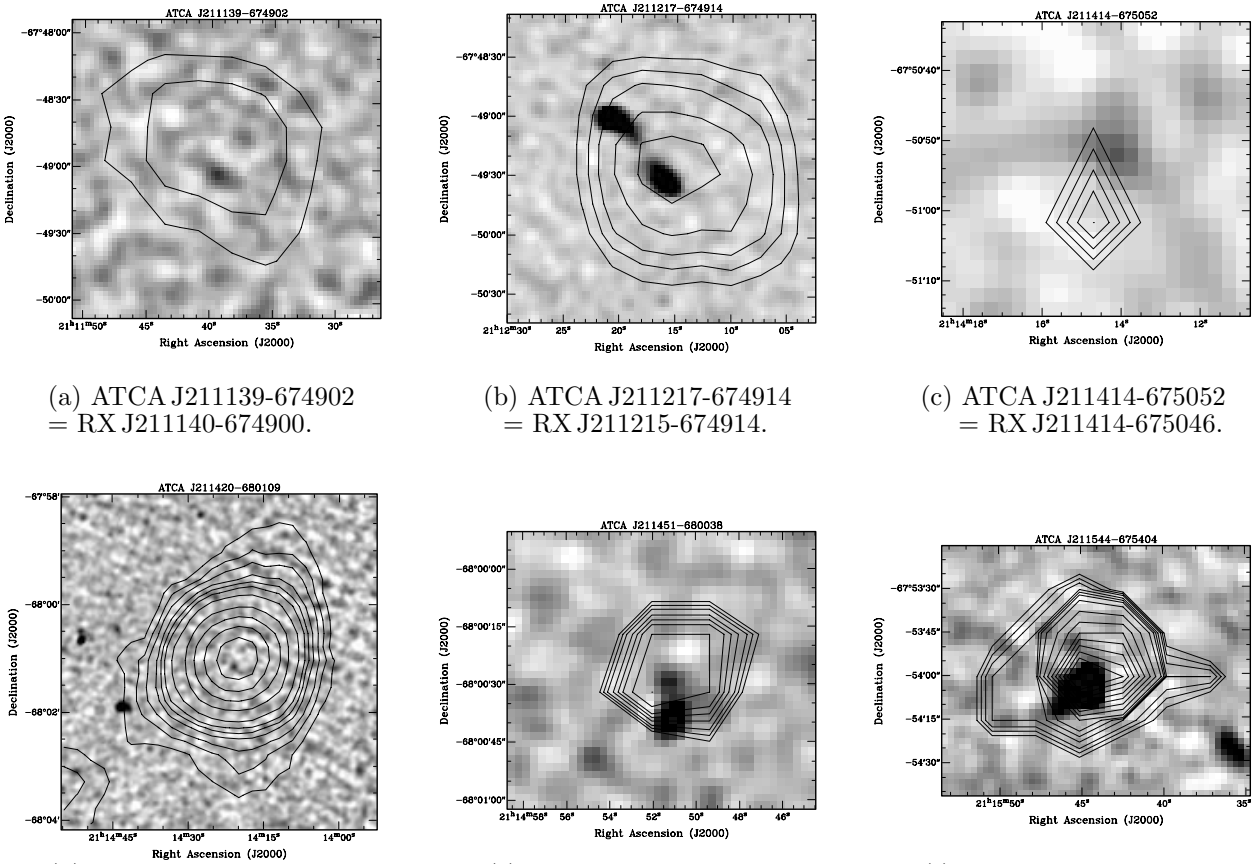

(a) ATCA J211139-674902 = RX J211140-674900.

(b) ATCA J211217-674914 = RX J211215-674914.

(c) ATCA J211414-675052 = RX J211414-675046.

(d) ATCA J211420-680109 = RX J211420-680108.

(e) ATCA J211451-680038 = RX J211451-680032.

(f) ATCA J211544-675404 = RX J211544-675403.

Fig. 2. *Images of six sources in common to radio-continuum and X-ray surveys of the Pavo deep field. The ATCA 20-cm images of Pavo deep field (grey-scale) are overlaid with contours from the ROSAT hard band observations. Contours of the ROSAT image are: 1.3, 1.5, 1.7, 2, 2.25, 2.5, 3, 4, 5, 6, 7, 8, 9 and 10 in units of 10^{-4} ROSAT PSPC counts s^{-1} $arcmin^{-2}$.*

The *IRAS* 100-μm images of Schlegel, Finkbeiner and Davis (1998) are a good tracer of low velocity ($\leq$75 km s^{-1}) galactic disk H I (Reach, Wall and Odegard 1998). Regions of higher velocity ($\geq$75 km s^{-1}) H I clouds are known to have low 100 μm emissivity, meaning 100-μm *IRAS* images are insensitive to the detection of higher velocity H I clouds and so the column density could be underestimated (Wakker and Boulanger 1986). The observed H I profiles of Cleary, Haslam and Heiles (1979) and Colomb, Poppel and Heiles (1980) for the Pavo field show all emission is confined to a velocity range of $\pm$30 km s^{-1}. We searched the observed H I profiles of Putman and Gibson (1999) and Putman et al. (2001) based on the Parkes H I All Sky Survey (Barnes et al. 2001) for high velocity clouds, but found no evidence out to velocities of 500 km s^{-1}. At the position of the Pavo field a value of N_H=(3.0$\pm$0.7)$\times10^{20}$ atoms cm^{-2} was calculated by scaling (Schlegel, Finkbeiner and Davis 1998) the 100-μm sky brightness by 1.49$\pm$0.24$\times10^{-20}$. Other surveys such as the CDFS estimate N_H=0.8$\times10^{20}$ cm^{-2} (Rosati et al. 2001). Hence, the Pavo field is a good region to pursue deep X-ray surveys.

More accurate values of N_H will only become available when the IAR Southern Sky Survey (Arnal et al. 2000) is corrected for spillover and far field galactic plane contamination.

3. SOURCE IDENTIFICATION

The comparison of the ATCA radio and the *ROSAT* X-ray survey of the Pavo field resulted in the discovery of only six sources common to both surveys (Fig. 2). The comparison between the ATCA radio and DSS2/SuperCOSMOS optical surveys resulted in the discovery of 29 sources in common.

Comparison of the positional separations between the two close radio frequencies (1416 and

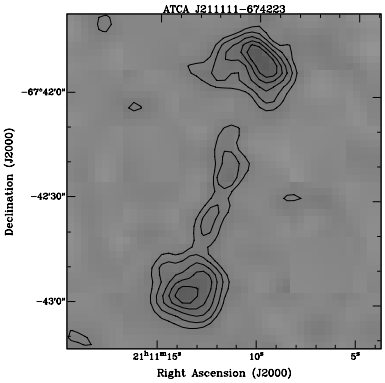

(a) ATCA J211111-674223. FR II with contours starting at 0.25 mJy.

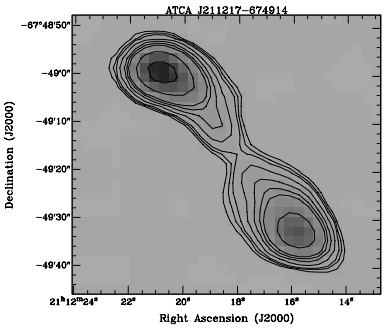

(b) ATCA J211217-674914. FR II.

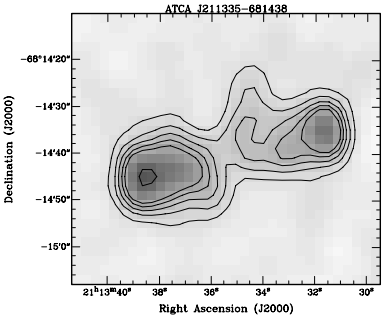

(c) ATCA J211335-681438. FR II with contours starting at 2.0 mJy and includes 20.0 mJy.

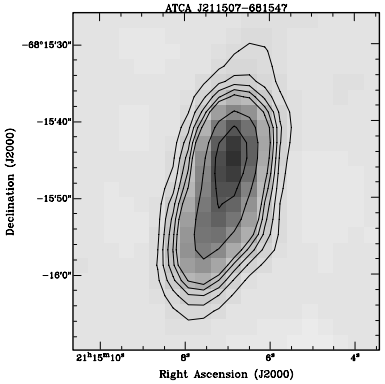

(d) ATCA J211507-681547. Image at 1416 MHz with contours starting at 2.0 mJy; also includes 20.0 and 30.0 mJy.

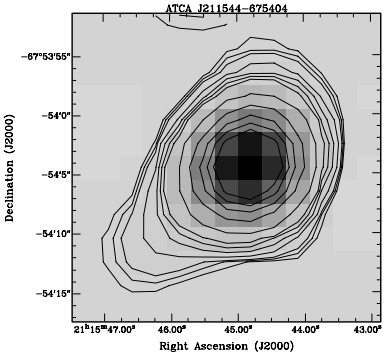

(e) ATCA J211544-675404.

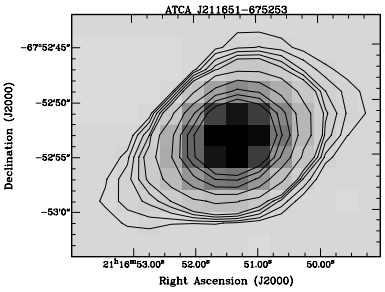

(f) ATCA J211651-675253. Contours start at 0.25 mJy.

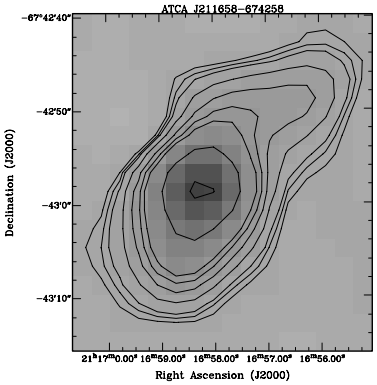

(g) ATCA J211658-674258.

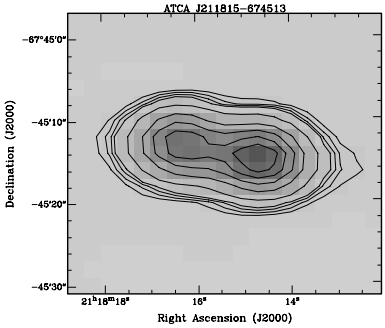

(h) ATCA J211815-674513. Contours start at 4.0 mJy; includes 20.0, 40.0, 60.0, 80.0 and 100.0 mJy.

Fig. 3. *Pavo very extended objects with contours at 1550 MHz. Unless otherwise stated contours are 0.15, 0.2, 0.25, 0.4, 0.6, 0.8, 1.0, 2.0, 4.0, 6.0, 8.0 and 10.0 mJy.*

1680 MHz) shows that all of the corresponding radio sources found at these two radio frequencies fall within 0.5″ of each other.

The positions are accurate to ∼10″ for X-ray sources from the *ROSAT* list. Therefore, we have searched an error circle of radius 10″ for radio counterparts of the *ROSAT* X-ray sources, finding six sources in common (see Figs. 2, 3 and 4).

The number of chance ATCA/*ROSAT* correlations was determined by positionally correlating the *ROSAT* X-ray source list with 300 randomly generated radio source lists. Each random radio list was selected to have the same source density, number of sources and sensitivity as the original ATCA source list. Within a search circle of 10″ only one source was found to be due to chance association.

Each radio counterpart was then visually examined in combination with DSS2 and SuperCOSMOS optical data to find any radio emission associated with a galaxy or AGN core. All optical or radio core counterparts should be within a combined position error radius of 2.8″ (95% confidence). Of the 93 ATCA sources in Table 2 — 29 have a SuperCOSMOS optical counterpart to the UK Schmidt plate limit of approximately m_J=23. This result is consistent with Benn et al. (1993) who find ∼20-30% of sub-mJy radio sources have optical counterparts with $m_J < 23$.

Some four sources (Table 2; sources N$^{\underline{o}}$ 19, 54, 61 and 73) from the radio catalogue were identified at all three frequencies i.e. X-ray, optical and radio (see Figs. 2(a)/4(c), 2(d)/4(l), 2(e)/4(o) and 2(f)/3(e)/4(u)).

Radio source N$^{\underline{o}}$ 73 (ATCA J211544-675404) is previously classified as a certain QSO (Danziger and Gilmozzi 1997). Sources ATCA J211217-674917 (N$^{\underline{o}}$ 27) and ATCA J211451-680032 (N$^{\underline{o}}$ 54) are AGN candidates based on the radio appearance. In a vicinity of source ATCA J211420-680109=RX J211420-680108 we can identify several radio and optical objects and therefore we classify this object as a galaxy cluster candidate. Source (ATCA J211139-674902) can be identified at optical frequencies and therefore is more likely to be a QSO. The remaining one source is a star-forming galaxy candidate. Further spectroscopic observations will reveal its intrinsic nature.

Table 5. Summary of the number of X-ray/Radio associations.

Radio	X-ray Surveys		Optical Surveys
Surveys	*Einstein*	*ROSAT*	DSS2 and SuperCOSMOS
ATCA	2	6	29
MOST	1	3	10

A positional correlation of the MOST and final ATCA catalogues (Table 2) showed only one MOST source (near the MOST 5σ detection limit) had no ATCA counterpart.

The number of correlations is summarised in Table 5 for the *ROSAT* and *Einstein* sample. The one *Einstein*/MOST correlation is repeated in the six ATCA/*ROSAT* correlations. For the three MOST/*ROSAT* only two were found in the ATCA/*ROSAT* correlations. The other MOST source was not detected in the final ATCA 20 cm images.

4. SOURCE INTENSITY COMPARISON

We have compared the X-ray source intensity (count rate, Table 3, Col. 6) with the radio flux density from Table 2 (Col. 4) for the six sources in common to both surveys. Most of the radio sources in the Pavo field fall below the sensitivity limit of the *ROSAT* survey (below 0.002 cts s^{-1}) while most of the X-ray sources fall below the sensitivity limit of the radio survey (below $3\sigma \approx 0.15$ mJy). Many strong radio sources and strong X-ray sources have not been detected at X-ray and radio frequencies, respectively.

Only 10 sources are in common to X-ray and optical (SuperCOSMOS) surveys of the Pavo field. As for the X-ray–to–radio comparison we could not find obvious correlations between X-ray count rates and optical magnitude for these 10 sources in common in the Pavo field.

We find 29 sources in common to radio-continuum and optical surveys of the Pavo field. Similarly as for the previous comparison, we find no correlation between radio flux density and optical magnitude.

5. INTERESTING OBJECTS IN THE PAVO FIELD

The Pavo Deep field contains many interesting objects as shown in Figs. 2, 3 and 4. The very extended sources (Fig. 3) were visualized using ATCA combined images to create a 1550 MHz field which were then overlaid with corresponding contours. Figures 4 were created using DSS2 optical images overlaid with 1550 MHz ATCA contours. We now discuss some of these objects.

ATCA J211111-674223 (Fig. 3(a)) appears to be a FR II AGN with two large lobes, an unresolved central core region, a jet and partial counter-jet. Although there are no definite hot spots, the jet does show a possible knot. The core of this double coincides with a magnitude m_J=20.54 optical object as shown in Fig. 4(a).

ATCA J211217-674914 (Figs. 2(b) and 3(b)) is also a double source with no obvious core or clear jet, possibly due to the orientation of the object to our line of sight. It is associated with an X-ray source (1.48 counts ks^{-1}) located not at the core, but in a central position of one of the lobes.

ATCA J211335-681438 (Fig. 3(c)) is an interesting FR II AGN with a curved jet like structure which may be due to orientation versus interactions with the intergalactic medium or its host galaxy although no optical counterpart is found. It has a fairly steep spectral index of $\alpha = -1.4$.

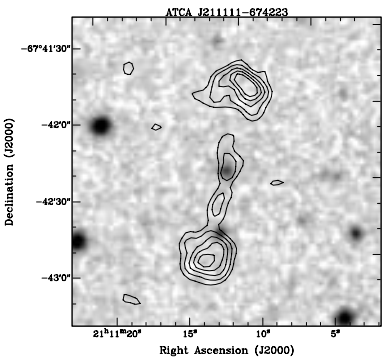

(a) ATCA J211111-674223. FR II with contours starting at 0.25 mJy.

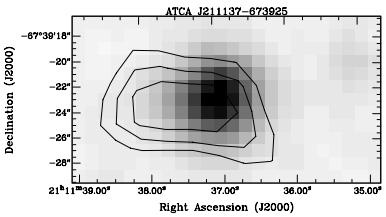

(b) ATCA J211137-673925. Contours start at 0.2 mJy.

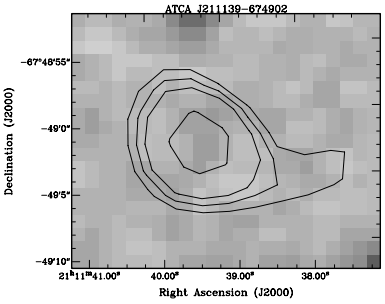

(c) ATCA J211139-674902.

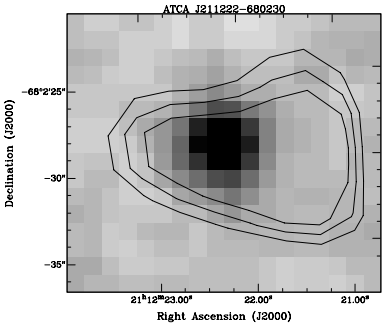

(d) ATCA J211222-680230.

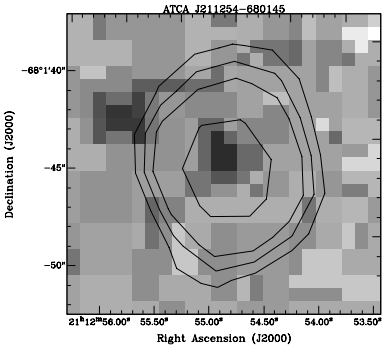

(e) ATCA J211254-680145. UKST blue versus ATCA contours at 1416 MHz.

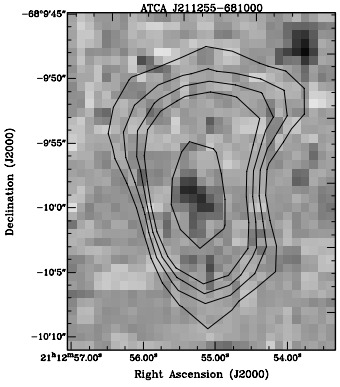

(f) ATCA J211255-681000. UKST blue versus ATCA contours starting at 0.4 mJy.

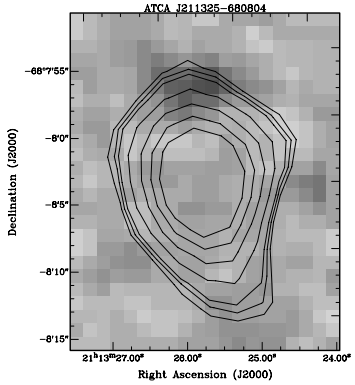

(g) ATCA J211325-680804.

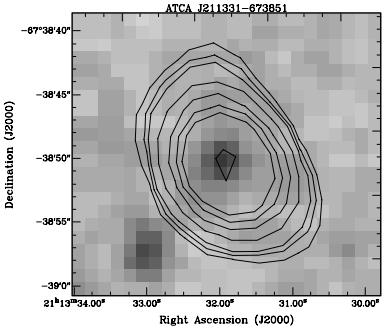

(h) ATCA J211331-673851.

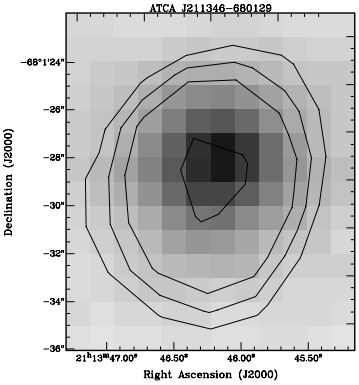

(i) ATCA J211346-680129.

Fig. 4. *DSS2 red images (except for a few objects in which it was necessary to use UKST blue images) with ATCA contours at 1550 MHz. Unless otherwise stated contours are 0.15, 0.2, 0.25, 0.4, 0.6, 0.8, 1.0, 2.0, 4.0, 6.0, 8.0, 10.0 mJy.*

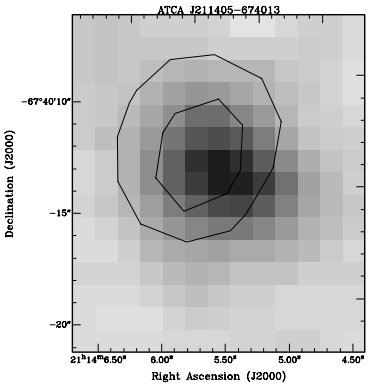

(j) ATCA J211405-674013.

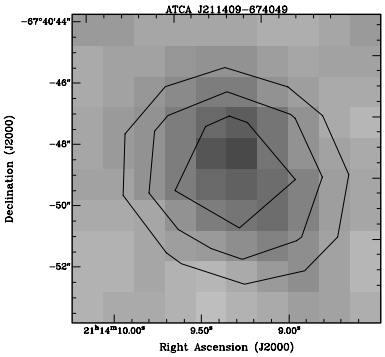

(k) ATCA J211409-674049.

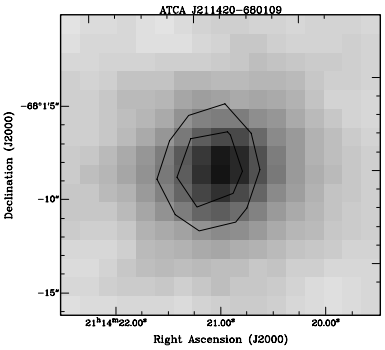

(l) ATCA J211420-680109.

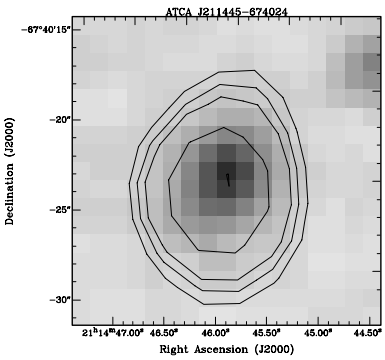

(m) ATCA J211445-674024.

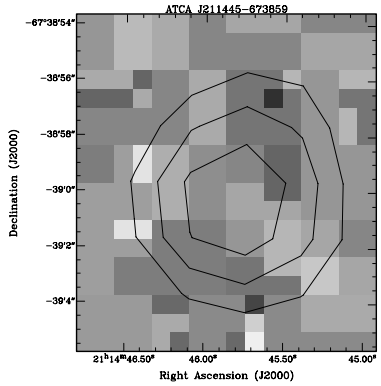

(n) ATCA J211445-673859. UKST blue versus ATCA contours.

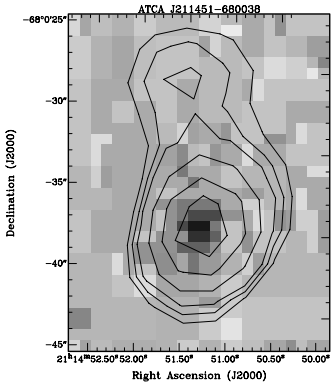

(o) ATCA J211451-680038. UKST blue versus ATCA contours.

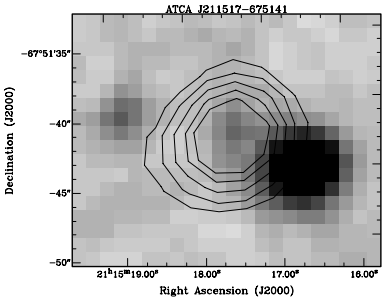

(p) ATCA J211517-675141. Contours start at 0.25 mJy.

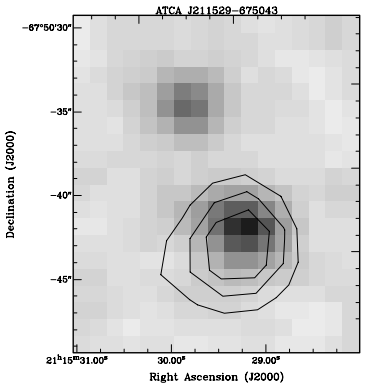

(q) ATCA J211529-675043. Image is at 1416 MHz.

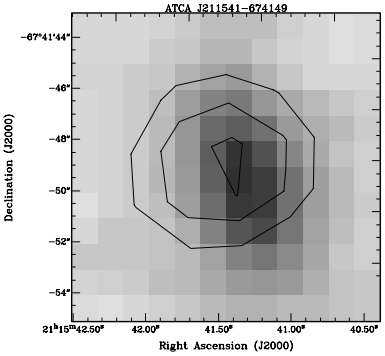

(r) ATCA J211541-674149.

Fig. 4. (Continued) *DSS2 red images (except for a few objects in which it was necessary to use UKST blue images) with ATCA contours at 1550 MHz. Unless otherwise stated contours are 0.15, 0.2, 0.25, 0.4, 0.6, 0.8, 1.0, 2.0, 4.0, 6.0, 8.0, 10.0 mJy.*

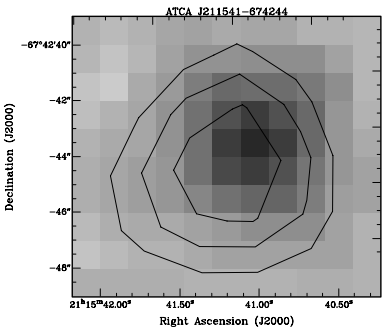

(s) ATCA J211541-674244.

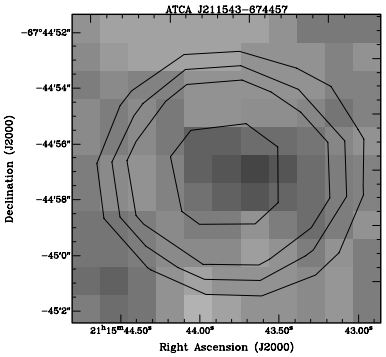

(t) ATCA J211543-674457.

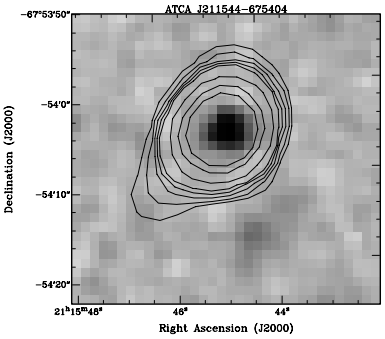

(u) ATCA J211544-675404. Contours start at 0.25 mJy.

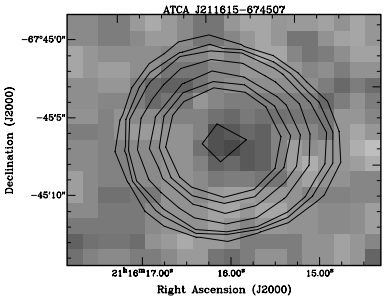

(v) ATCA J211615-674507.

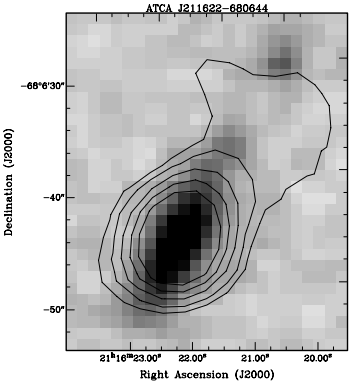

(w) ATCA J211622-680644. Contours start at 0.25 mJy.

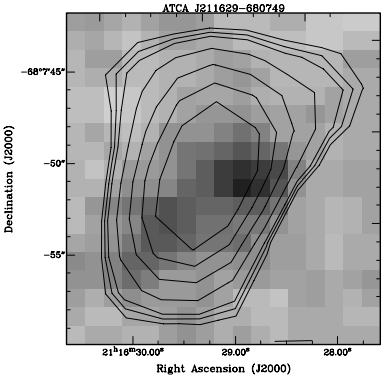

(x) ATCA J211629-680749.

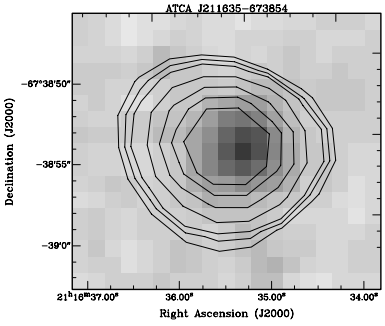

(y) ATCA J211635-673854.

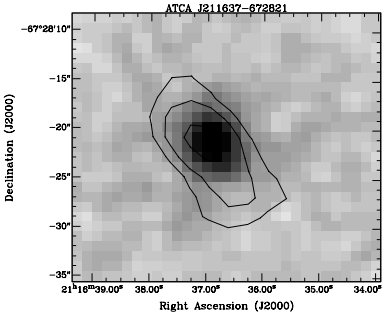

(z) ATCA J211637-672821. Image at 1416 MHz with contours starting at 0.25 mJy.

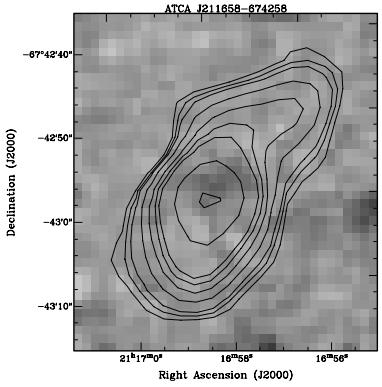

(z1) ATCA J211658-674258.

Fig. 4. (Continued) *DSS2 red images with ATCA contours. Unless otherwise stated contours are 0.15, 0.2, 0.25, 0.4, 0.6, 0.8, 1.0, 2.0, 4.0, 6.0, 8.0, 10.0 mJy at 1550 MHz.*

ATCA J211507-681547 and ATCA J211815-674513 (Figs. 3(d) and 3(h)) are double lobe extended objects with similar spectral indexes of about $\alpha = -1$.

ATCA J211815-674513 (Fig. 3(h)) is also known as PKS 2113-679 (see earlier discussion) and has a spectral index of $\alpha = -0.8$ listed in the NASA/IPAC Extragalactic Database, NED. This is consistent with our estimated value of $\alpha = -1.0 \pm 0.2$.

ATCA J211544-675404 (Figs. 2(f) and 3(e)) has a spectral index of $\alpha = -0.3$, more consistent with a compact source with weaker extended features. It has a strong X-ray counterpart (8.14 counts ks^{-1}) located near the center of the source along with an optical component of magnitude m_J=19.34. The latter is a known quasar, HB89 2111-681 with a redshift of 1.13.

ATCA J211651-675253 (Fig. 3(f)) also has a relatively flat spectral index of $\alpha = -0.5$, but no X-ray or optical counterparts were found to be associated with it.

ATCA J211658-674258 (Fig. 3(g)) is a more extended object with a more typical radio lobe spectral index of $\alpha = -0.9$. There is an optical component (Fig. 4(z1)) with magnitude m_J=20.0 present.

ATCA J211420-680109 (Figs. 2(d) and 4(l)) is an interesting source that correlates to VMF98 201, a galactic cluster with a redshift of 0.15 and a heliocentric radial velocity of 44 969 km s^{-1}. The cluster has a magnitude of m_J=17.37 and is a strong X-ray source with 9.07 counts ks^{-1}.

6. CONCLUSIONS

Observations of the Pavo field were made with the ATCA at 20 cm in 1992, reaching a flux density limit of ∼50 μJy (rms). The low radio source density ensures a chance coincident rate of <2% for the *ROSAT* position errors and the arcsecond radio positions allow for efficient optical identification. We found 93 radio sources above flux limit of $S_{1.4\ \mathrm{GHz}}$ >0.25 mJy. The *ROSAT* X-ray observations detected 69 sources in a similar area.

A total of only six radio sources are located within 10″ of the *ROSAT* X-ray positions compared to the 1′ radius used by Hamilton and Helfand (1993). We find that at separations of <10″ two of these sources are identified with a QSO, two with FR II AGNs and one with a galaxy cluster. The remaining one source in common to the two surveys could be associated by random chance or it could be a star-forming candidate. However, we do not know if this system may actually contain a supermassive black hole with accretion the primary mechanism for X-ray emission. Therefore, we conclude that Hamilton and Helfand (1993) prediction that faint radio selected galaxies are a new class contributing to the diffuse X-ray background (XRB) radiation is unlikely at $S_{0.08-2.4\ \mathrm{keV}} > 6 \times 10^{-15}$ erg cm^{-2} s^{-1}.

Also, we estimate for the Pavo field the N_H to be (3.3±0.7)×10^{20} cm^{-2} which is somewhat higher than the CDFS survey (N_H=(0.8±3.0)×10^{20} cm^{-2}).

Ever since Hamilton and Helfand (1993) it has been almost assumed by "common sense" that the soft X-ray background is significantly contributed to by star-forming systems at flux detections greater than ∼10^{-14} erg cm^{-2} s^{-1}. Certainly, with greater sensitivity, newer X-ray instruments will detect weaker X-ray sources including those related to starburst activity. Thus far, however, the case is not strong that sensitivity has been reached even with 90% of the XRB resolved. Even if a starburst system is associated with significant X-ray emission, there is mounting evidence that some of these objects contain hidden AGN actually responsible for most current X-ray detections. Certainly, our data does not bear out the idea that 20% of the XRB (soft) is from activity related to starburst systems.

Acknowledgements – We used the Karma/MIRIAD software package developed by the ATNF and the EXSAS/MIDAS software package developed by the MPE. The *ROSAT* project is supported by the German BMBF and the MPG. Photographic data were obtained using the UK Schmidt Telescope. The UK Schmidt Telescope was operated by the Royal Observatory Edinburgh, with funding from the UK Science and Engineering Research Council, until 1988 June, and thereafter by the Anglo-Australian Observatory. Original plate material is copyright (c) the Royal Observatory Edinburgh and the Anglo-Australian Observatory. The plates were processed into the present compressed digital form with their permission. The DSS was produced at the STScI under US Government grant NAG W-2166. This work was part of the final semester project of the Astronomy Internet Masters (AIM) course at the University of Western Sydney by B.C.P. Borun, J. Payne, M. Dionne, M. Ganis and M. Ognjanović. We thank L. Staveley-Smith (ATNF) for the help in N_H estimate of the Pavo field.

REFERENCES

Arnal, E.M., Bajaja, E., Larrarte, J.J., Morras, R. and Pöppel, W.G.L.: 2000, *Astron. Astrophys. Suppl. Series*, **142**, 35.

Barnes, D.G. et al.: 2001, *Mon. Not. Roy. Astron. Soc.*, **322**, 486.

Bedding, T.R. and Turtle A.J.: 1990, *Proc. ASA*, **8**, 348 (BT90).

Benn, C.R., Rowan-Robinson, M., McMahon, R.G., Broadhurst, T.J. and Lawrence A.: 1993, *Mon. Not. Roy. Astron. Soc.*, **263**, 98.

Boldt, E.A. and Leiter, D.: 1987, *Astrophys. J.*, **322**, L1.

Boulanger, F., Abergel, A., Bernard, J.-P., Burton, W.B., Desert, F.-X., Hartmann, D., Lagache, G. and Puget, J.-L.: 1996, *Astron. Astrophys*, **312**, 256.

Boyle, B.J., Staveley-Smith, L., Stewart, G.C., Georgantopoulos, I., Shanks, T. and Griffiths, R.E.: 1993, *Mon. Not. Roy. Astron. Soc.*, **265**, 501.
Cash, W.: 1979, *Astrophys. J.*, **228**, 939.
Cleary, M.N., Haslam, C.G.T. and Heiles, C.: 1979, *Astron. Astrophys. Suppl. Series*, **36**, 95.
Colomb, F.R., Poppel, W.G.L. and Heiles, C.: 1980, *Astron. Astrophys. Suppl. Series*, **40**, 47.
Cruddace, R.G., Hasinger, G. and Schmitt, J.H.M.M.: 1988, in: Astronomy from Large Databases, eds. Murtagh F., Heck A., p. 177.
Danziger, I.J. and Gilmozzi, R.: 1997, *Astron. Astrophys.*, **323**, 47.
Dickey, J.M. and Lockman, F.J.: 1990, *Ann. Rev. Astron. Astrophys.*, **28**, 215.
Fabian, A. and Barcons, X.: 1992, *Ann. Rev. Astron. Astrophys.*, **30**, 429.
Garrett et al.: 2000, in: EVN Symposium 2000, Proceedings of the 5th european VLBI Network Symposium, eds. Conway, J.E., Polatidis, A.G., Booth, R.S. and Pihlström, Y.M., p. 137.
Garrett, M.A.: 2001, *Astron. Astrophys.*, **366**, L5.
Giacconi, R. et al.: 1962, *Phys. Rev. Lett.*, **9**, 439.
Giacconi, R. et al.: 1979a, *Astrophys. J.*, **230**, 540 (a).
Giacconi, R. et al.: 1979b, *Astrophys. J.*, **234**, L1 (b).
Giacconi, R. et al.: 2001, *Astrophys. J.*, **551**, 624.
Gregory, P.C., Vavasour, J.D., Scott, W.K., Condon, J.J.: 1994, *Astrophys. J. Suppl. Series*, **90**, 173.
Griffiths R.E. et al.: 1983, *Astrophys. J.*, **269**, 375.
Griffiths, R.E., Tuohy, I.R., Brissenden, R.J.V. and Ward M.: 1992, *Mon. Not. Roy. Astron. Soc.*, **255**, 545.
Hamilton, T., Helfand, D.J. and Wu, X.: 1991, *Astrophys. J.*, **379**, 576.
Hamilton, T. and Helfand, D.J.: 1993, *Astrophys. J.*, **418**, 55.
Hasinger, G., Trümper J. and Schmidt, M.: 1991, *Astron. Astrophys.*, **246**, L2.
Hasinger, G.: 1993, *Adv. Space Res.*, **13**, 241.
Hasinger, G., Burg, R., Giacconi, R., Schmidt, M., Trümper, J. and Zamorani, G.: 1998, *Astron. Astrophys.*, **329**, 482.
Hornschemeier, A.E. et al.: 2001, *Astrophys. J.*, **554**, 742.
Kellermann, K.I, Fomalont, E.B., Rosati, P., Shaver, P., CDFS Collaboration : 2000, *Bull. American Astron. Soc.*, **197** (90.02).
Kron, R.G., Koo, D.C. and Windhorst, R.A.: 1985, *Astron. Astrophys.*, **146**, 38.
Marshall, F., Boldt, E.A., Holt, S.S., Miller, R.B., Mushotzky, R.F. and Rose, L.A.: 1980, *Astrophys. J.*, **235**, 4.
Mather, J.C. et al.: 1990, *Astrophys. J.*, **354**, L37.
McCammon, D. and Sanders, W.T.: 1990, *Ann. Rev. Astron. Astrophys.*, **28**, 657.
Murray, S.S.: 1981, The Einstein Observatory – An X-ray Eye in the Sky, Science Year, World Book.
Mushotzky, R.F., Cowie, L.L., Barger, A.J. and Arnaud, K.A.: 2000, *Nature*, **404**, 459.
Primini, F.A., Murray, S.S., Huchra, J., Schild, R., Burg, R. and Giacconi, R.: 1990, *Astrophys. J.*, **374**, 440.
Putman, M.E. and Gibson, B.K.: 1999, *Proc. ASA*, **16**, 70.
Putman M.E. et al.: 2001, astro-ph/10416
Reach, W.T., Wall, W.F. and Odegard, N.: 1998, *Astrophys. J.*, **507**, 507.
Rosati, P. et al. 2001, *Astrophys. J.*, **566**, 667.
Sault, R. and Killeen, N.: 1999, MIRIAD Users Guide, ATNF.
Schlegel, D.J., Finkbeiner, D.P. and Davis, M.: 1998, *Astrophys. J.*, **500**, 525.
Shanks, T., Georgantopoulos, I., Stewart, G.C., Boyle, B.J. and Griffiths, R.E.: 1991, *Nature*, **353**, 315.
Stocke, J.T., Morris, S.L., Gioia, I.M., Maccacaro, T., Schild, R., Wolter, A., Fleming, T.A. and Henry, J.P.: 1991, *Astrophys. J. Suppl. Series*, **76**, 813.
Thuan, T.X. and Condon, J.J.: 1987, *Astrophys. J.*, **322**, L9.
Tozzi, P. et al.: 2001, *Astrophys. J.*, **562**, 42.
Trümper, J.: 1982, *Adv. Space Res.*, **2**, 241.
Wakker, B.P. and Boulanger, F.: 1986, *Astron. Astrophys.*, **170**, 84.
Windhorst, R.A., Fomalont, E.B., Kellermann, K.I., Partridge, R.B., Richards, E., Franklin, B.E., Pascarelle, S.M. and Griffiths, R.E.: 1995, *Nature*, **375**, 471.
Wright, A.E., Griffith, M., Burke, B. and Ekers, R.D.: 1994, *Astrophys. J. Suppl. Series*, **91**, 111.
Zamorani, G. et al.: 1999, *Astron. Astrophys.*, **346**, 731.

ИЗУЧАВАЊЕ PAVO ДУБОКОГ ПОЉА НА ВИШЕ ФРЕКВЕНЦИЈА

М. Д. Филиповић[1,2], М. Андерсон[1,2], Р. Д. Екерс[2], И. Ј. Данзигер[3], Х-У. Цимерман[4], Г. Л. Вајт[2], П. А. Џонс[2], Б. Ц. П. Борун[1], Ј. Л. Пејн[1], М. Дионе[1], М. Ганис[1,5] и М. Огњановић[1]

[1] *University of Western Sydney, Locked Bag 1797 Penrith South, DC NSW 1797 Australia*

[2] *Australia Telescope National Facility, CSIRO, P.O. Box 76, Epping, NSW 2121 Australia*

[3] *Osservatorio Astronomico di Trieste, Via Tiepolo 11, I-34131 Trieste, Italia*

[4] *Max-Planck-Institut für extraterrestrische Physik, Giessenbachstraße, D-85740 Garching, Deutchland*

[5] *Pace University, 861 Bedford Road, Pleasantville NY 10532, USA*

UDK 524.82
Оригинални научни рад

У овој студији тестирамо предвиђање Хамилтона и Хелфанда (1993) да су изабране слабе радио галаксије нова класа објеката који значајно доприносе дифузној позадинској радијацији у X подручју (XRB – X-ray background). Тестирање је базирано на корелацији између X, оптичких и радио позиција објеката детектованих са ROSAT ($S_{0.08-2.4keV} > 6 \times 10^{-15}$ erg cm^{-2} s^{-1}; 69 објеката) и ATCA ($S_{1.42GHz}$ >250 μJy; 93 објекта) посматрања тзв. Ајнштајн Паво поља. Укупно шест ATCA радио објеката налазе се унутар ROSAT-ове позиционе грешке посматрања од 10″, а само један од њих се може приписати случајном појављивању. Према томе, пет X објеката су радио емитери. Четири од горе наведених шест објеката су заједнички за радио и X прегледе а и идентификовани су на оптичким фреквенцијама где је један већ одранише познати квазар (ATCA J211544-675404). Објекат ATCA J211139-674902, види се на оптичким фреквенцијама и због тога је веома вероватно - квазар. Два објекта (ATCA J211217-67491 и ATCA J211451-680038) су одлични кандидати за Активна Галактичка Језгра (AGN). Радио и X објекат ATCA J211420-680109=RX J211420-680108 је кандидат за јато галаксија. И последњи објекат ATCA J211414-675052 је кандидат за 'стар-форминг' галаксију подразумевајући да није случајна корелација (појављивање). Иако је статистички узорак мали, ова студија не подржава постулат да су 'стар-форминг' галаксије значајни доприносиоци популацији 'меких' X објеката. Из овога следи да је учешће X објеката који имају и радио емисију у дифузном XRB зрачењу на нивоу од највише пар процената $S_{0.08-2.4\ \mathbf{keV}} > 6 \times 10^{-15}$ erg cm^{-2} s^{-1}.